

Dynamic Experiments: An Overview

W.J. Nellis

This article was submitted to International School of Physics "Enrico Fermi" Course on: "High Pressure Phenomena", Varenna, Italy, July 3-13, 2001

July 6, 2001

U.S. Department of Energy

Lawrence
Livermore
National
Laboratory

DISCLAIMER

This document was prepared as an account of work sponsored by an agency of the United States Government. Neither the United States Government nor the University of California nor any of their employees, makes any warranty, express or implied, or assumes any legal liability or responsibility for the accuracy, completeness, or usefulness of any information, apparatus, product, or process disclosed, or represents that its use would not infringe privately owned rights. Reference herein to any specific commercial product, process, or service by trade name, trademark, manufacturer, or otherwise, does not necessarily constitute or imply its endorsement, recommendation, or favoring by the United States Government or the University of California. The views and opinions of authors expressed herein do not necessarily state or reflect those of the United States Government or the University of California, and shall not be used for advertising or product endorsement purposes.

This is a preprint of a paper intended for publication in a journal or proceedings. Since changes may be made before publication, this preprint is made available with the understanding that it will not be cited or reproduced without the permission of the author.

This work was performed under the auspices of the United States Department of Energy by the University of California, Lawrence Livermore National Laboratory under contract No. W-7405-Eng-48.

This report has been reproduced directly from the best available copy.

Available electronically at <http://www.doc.gov/bridge>

Available for a processing fee to U.S. Department of Energy
And its contractors in paper from
U.S. Department of Energy
Office of Scientific and Technical Information
P.O. Box 62
Oak Ridge, TN 37831-0062
Telephone: (865) 576-8401
Facsimile: (865) 576-5728
E-mail: reports@adonis.osti.gov

Available for the sale to the public from
U.S. Department of Commerce
National Technical Information Service
5285 Port Royal Road
Springfield, VA 22161
Telephone: (800) 553-6847
Facsimile: (703) 605-6900
E-mail: orders@ntis.fedworld.gov
Online ordering: <http://www.ntis.gov/ordering.htm>

OR

Lawrence Livermore National Laboratory
Technical Information Department's Digital Library
<http://www.llnl.gov/tid/Library.html>

Dynamic Experiments: an Overview

W. J. Nellis

University of California
Lawrence Livermore National Laboratory
Livermore, California 94550

I. INTRODUCTION

Dynamic high pressures are applied rapidly to materials to increase density and temperature, to alter crystal structure and microstructure, and to change physical and chemical properties [1]. These effects are achieved at high pressures and many are retained on release from high pressures. Today it is possible to achieve pressures of order 50 to 500 GPa (5 Mbar), compressions up to fifteen fold greater than initial solid density in the case of hydrogen, and temperatures ranging from 1 K up to several eV (11,600 K) in condensed matter. At these extreme conditions the bonding, structure, physical properties and chemistry of condensed matter are changed substantially from what they are at ambient. This in turn opens up a whole new range of opportunities for novel condensed matter physics, chemistry, and planetary research at extreme conditions. If high pressure phases could be quenched to ambient, then new opportunities would become available in condensed matter and material sciences, as well as for technological applications.

This article is concerned with high pressures achieved dynamically by shock compression [2]. In fact, the terms dynamic and shock are used interchangeably to describe pressure pulses above 1 GPa (10 kbar) or so. Because dynamic compression is so fast, the process is adiabatic and temperature increases. Shock compression is achieved by high velocity impact obtained with light-gas guns (two-stage, single-stage, and powder guns), pulsed lasers, high pulsed electrical currents, and explosives. In this article we are concerned with strong shock compressions; that is, those which occur in a time of the order of a ps and for which the pressure exceeds 1 GPa. Typical durations of the pressure pulse are a few 100 ns, a few ns, a few 10 ns, and a few 1000 ns for guns, lasers, pulsed currents, and explosives, respectively.

Isentropic compression experiments (ICE) are performed today using high pulsed currents in which pressure rises in a few ns [3]. This relatively long risetime decreases the temperature and increases the density compared to what would be obtained by a single shock to the same

final pressure. As a result the ICE process is essentially isentropic, rather than a shock. This situation demonstrates how thermodynamic states achieved are very sensitive to the rise time and shape of the pressure pulse. In this case, increasing the rise time of a pressure pulse from essentially instantaneous rise time for a shock to just a few ns greatly reduces temperature and increases density achieved.

Sample sizes range from 20 mm diameter for two-stage light-gas gun experiments down to several tens to hundreds of microns for laser experiments. A wide range of electrical, optical, and x-ray properties are measured in the brief time durations and small sample dimensions.

If a specimen material is in bulk thermodynamic equilibrium at both dynamic and static high pressures, data from the two types of experiments are related by a thermal model. Because of this, all primary pressure scales at static high pressures above 7 GPa are derived from shock-wave Hugoniot equation-of-state (EOS) data.

On release of shock pressure, very high quench rates up to 10^{12} bar/s and 10^9 K/s are achieved, which can cause retention of high pressure phases metastably at ambient. These quench rates are the maxima in macroscopic specimens because they occur at the speed of sound. Materials made using dynamic high pressures are nanoscale because of the short time scales. Results obtained with gas guns and explosives can often be scaled up in size using large explosively driven systems. Pressures and temperatures obtained with a diamond anvil cell can often be obtained with larger samples using multiple-shock compression or ICE compression.

II. Shock Compression

The macroscopic structure of a shock wave depends on phenomena such as elastic limits, phase transitions, shock reverberations caused by reflections at interfaces between dissimilar materials, and the shape of the shock compression curves of the materials involved. That is, shock velocity depends on the slope of the shock compression curve in pressure-volume space. This slope changes discontinuously at elastic limits and often at phase transitions and it changes continuously within a given phase. In a simple fluid shock pressure is determined by the incident driving pressure and the compressibilities and shock impedances of the materials involved. Dynamic pressures can only sense phenomena which occur during the time of the pressure pulse.

Temperatures achieved in shock compression are determined by choice of shock pressure, sample material, initial sample density and temperature (interrelated), and shock-wave structure. The highest

temperature at a given pressure is achieved by a single shock to that pressure. A pulse with several step rises in pressure caused by shock reverberation between stiff anvils causes a lower final shock temperature and higher density than a single shock to the same final pressure. In fact, a reverberating shock causes a quasi-isentropic compression. By taking various phenomena into account, the macroscopic shape of a shock wave can be tuned and, thus, the temperature achieved can be tuned as well. Perhaps, the greatest advance in shock compression technology today is the ability to tune temperature at fixed pressure. One of the consequences is the ability to achieve the same thermodynamic states in dynamic and static high pressure experiments for the first time.

II.A Simple Shock Waves

A simple shock is essentially a discontinuity in flow and thermodynamic variables which propagates through a specimen at a supersonic velocity, called shock velocity. A simple, one-dimensional shock front involves a single sharp step rise in shock pressure and other variables in going from an unshocked or from one shocked state to another shocked state. A simple shock front is illustrated in **Fig. 1a**, where P_H is shock pressure, V_H is specific shock volume, E_H is specific internal shock energy, u_s is shock velocity, u_p is mass velocity behind the shock front, and x is distance. The zero-subscripted variables are initial values ahead of the shock front.

The shock front is not a perfect discontinuity. Rather, the shock front is the microscopic spatial region in which initial unshocked material goes completely to the equilibrated temperature and density of the shock-compressed state. Within the shock front, internal energy deposited by shock compression equilibrates among the various allowed compressional and internal energy modes (intermolecular repulsion, molecular dissociation, electronic excitations, etc). The spatial rise of a 1.2 GPa shock wave in liquid Ar is illustrated in **Fig. 1b** [4,5]. Intermolecular repulsion is the only degree of freedom in Ar at these conditions. The shock front in **Fig. 1b** has a width of 10 Å. At 6 GPa the width of the shock front Ar is also 10 Å but pressure undergoes a couple of small oscillations before equilibrating [6]. The width of a shock front is thicker for more degrees of freedom and is typically in the range 10 to 1000 Å, depending on material.

The rise time of shock pressure is the temporal width of the shock front. The temporal width is the time required for shock velocity to transit the width of a shock front. Depending on the material, the rise time of a shock could be much less or substantially more than a ps. The

risetime in **Fig. 1b** is ~ 0.5 ps because the shock velocity is 2 km/s. For a typical strong shock velocity of 10 mm/ μ s in a fluid, the temporal width in more complex systems ranges from a few 0.1 to 10 ps. The shape of a shock front is constant in time for a steady unrarefied wave. In solids the high rate of application of pressure is sufficiently high to generate high densities of lattice defects, densities which cannot be generated by other means.

Material is shocked directly along the Rayleigh line from (P_0, V_0) to (P_H, V_H) , as shown in **Fig. 2**. A plot of the locus of any two of these single-shock parameters is called the Hugoniot (see II.B), shock adiabat, or shock-compression curve. Typical representations are u_s versus u_p , which are determined in an experiment, and P_H versus V_H , which are derived from u_s versus u_p (see below).

The example in **Fig. 1** represents a simple wave in which all effects except the equation of state are said to be overdriven and so represents a shock wave in a fluid or a relatively high-pressure plastic wave in a solid. **Fig. 1** could also represent a purely elastic wave below the Hugoniot elastic limit (HEL) of a solid. P_{HEL} is the maximum shock pressure at which the material acts as an elastic solid in shock compression. In **Fig. 3(a)** P_B is the minimum pressure said to overdrive the HEL; that is, to have a single plastic wave with no sign of the HEL in the shock-wave profile. At intermediate pressures P_C between the HEL and P_B , a two-wave structure exists, as shown in **Fig. 3(b)**. In this case, a shock wave at intermediate pressure P_C splits into two waves, whose velocities are determined by the different slopes of the P_H – V_H curve in the two regimes in **Fig. 3(a)** (see II.B). The leading wave at P_{HEL} is called the longitudinal elastic precursor because its wave speed is higher than that of a plastic wave at a pressure P_C . At pressures above P_B the speed of the plastic wave exceeds that of the elastic wave at the HEL.

II.B. Rankine-Hugoniot Relations and Equations of State

The experimental design of shock-wave EOS experiments is based on the Rankine-Hugoniot equations, which are derived from conservation of momentum, mass, and energy across the front of a shock wave (**Fig. 1**). These equations are given by

$$P_H - P_0 = \rho_0 (u_s - u_0) (u_p - u_0), \quad (1a)$$

$$V_H = V_0 [1 - (u_p - u_0) / (u_s - u_0)], \quad (1b)$$

$$E_H - E_0 = 1/2 (P_H + P_0) (V_0 - V_H), \quad (1c)$$

where $\rho_H = 1/V_H$ is mass density and the other variables are defined in II.A. (P_H , V_H , E_H) data points are called Hugoniot data. For a single wave u_s is often measured; u_p is measured or is calculated using the shock impedance match principal, which states that P_H and u_p are continuous across an interface. Shock impedance is defined to be $\rho_0 u_s = P_H/u_p$, the slope of P_H versus u_p from Eq. (1a), where $P_0=u_0=0$. For a single strong shock, shock velocity is given by $u_s = V_0 [P_H / (V_0 - V_H)]^{1/2}$, i. e., shock velocity is proportional to the square root of the slope of the Rayleigh line. For the case of a symmetric impact in which an impactor of a given material is accelerated to velocity u_i and strikes a target of the same material, $u_p = u_i/2$ by symmetry. Eqs. 1 are the bases of all primary pressure scales above about 7 GPa, both static and dynamic.

For many solids and liquids in the absence of phase transitions, experimental Hugoniot data follow the relation:

$$u_s = C + S u_p, \quad (2)$$

where C is bulk sound speed at $P=0$ and S is the slope of the linear relation between u_s and u_p . The constant S is a function of the pressure derivative of the isentropic bulk modulus [7]. Eq. 2 can be used to calculate P_H , V_H , and E_H from Eq. (1). For comparison, the experimental Hugoniot curve and the theoretical 0-K isotherm and isentrope of Al are plotted in **Fig. 4** [8]. For strong shocks, the total specific internal energy of Eq. (1c) becomes $E = 1/2 P_H (V_0 - V_H)$. As shown in **Fig. 4**, the total specific internal energy is represented by the area of the triangle under the Rayleigh line. Internal energy caused by isentropic compression to the same volume is reversible and is represented by the area under the isentrope. Reversible internal energy is removed from the sample when pressure is released. Irreversible internal energy is, thus, represented by the dashed area in **Fig. 4**. This irreversible internal energy is the reason for shock-induced heating and is the reason why shock pressures cause higher thermal and total pressures than isothermal, static compression to the same volume. In addition to heating materials, irreversible shock energy is also available for inducing phase transitions, changing microstructures, causing chemical reactions, and absorption by internal degrees of freedom.

Single-shock EOS experiments with a two-stage gun are illustrated in **Fig. 5(a)**, in which a Ta impactor strikes a stepped Al target. Impactor velocity u_i and shock velocity u_s in the target are obtained by recording two flash radiographs of the impactor inflight at measured spatial and temporal intervals and by measuring the shock-transit time across the

measured step height. u_l and u_s and the shock-impedance-match principal determine (P_H, V_H, E_H) in the target with $u_o = 0$ in Eqs. (1). Double-shock EOS experiments are illustrated in **Fig. 5(b)**, in which a Ta impactor strikes a soft Al target backed by a stiff Ta anvil. After the first shock traverses the Al, it reflects backward off the stiffer Ta anvil, double-shocking the Al and sending a shock forward into the Ta anvil. By taking the first-shock state as the zero-subscripted variables in Eqs. (1), measuring u_l , and measuring u_s in the anvil, the second-shock state can be obtained from Eqs. (1). Double-shocking to a given volume produces lower pressures and temperatures than a single shock to the same volume.

Hugoniot EOS data for Al, Cu, and Ta have been measured up to a few 100 GPa using a two-stage light-gas gun at higher pressures and a planar explosive system at lower pressures [9]. Maximum Hugoniot pressures in these experiments are 170, 330, and 430 GPa for Al, Cu, and Ta, respectively [10].

II.C Thermal Equation of State and Static High Pressure Scales

Hugoniot EOS data provide a reference curve for calculating states off the Hugoniot. Below about 100 GPa, thermal pressure at a given volume can be calculated from the Gruneisen model, which assumes that $(\partial P / \partial E)_V = \gamma / V$ is a constant, where γ is the Gruneisen parameter which depends only on V . The classical Gruneisen model assumes that thermal energy is absorbed only by the lattice and that $\gamma = -d \vartheta / d \ln V$, where ϑ is the Debye temperature which depends on phonon frequencies [11]. Thermodynamic γ has been obtained by measuring various discrete (P, E) states at the same V and approximating differentials with differences. The latter can be obtained by single and double-shock data to the same volume using both solid and porous specimens. Porous specimens (powders and aerogels), with lower initial densities than solid ones, are more compressible and thus have larger internal energies and thermal pressures at a given volume than do shock-compressed crystal-density specimens. EOS data for porous and solid specimens of Al, Cu, and Fe suggested that γ / V is constant [12], the common form used for γ . Also, γ has been determined from sound speed measurements, described below (II.F). Heat capacities are estimated to calculate temperatures from internal energies.

More detailed theoretical calculations of the EOS of metals have been developed by Moriarty [13]. Electron band theory is used to calculate the 0-K isotherm in P - V space, to which is added electron-thermal and ion-thermal contributions to the pressure as functions of V and T .

Hugoniot EOS data are the primary data for static pressure scales above 7 GPa. The optical shift of ruby fluorescence and x-ray diffraction densities are calibrated versus 300-K P-V isotherms calculated from measured Hugoniots and the above thermal models. This process has been used up to the 500 GPa range, the current upper limit of static-pressure diamond-anvil-cell experiments [14]. Common x-ray markers used to determine pressure in a diamond anvil cell are Mo, Pt, and Cu.

II.D Shock Temperatures and Optical Emission Spectra

Shock temperatures have been measured in shocked transparent liquid and solid specimens by fitting the spectral dependence of radiation emitted from the shock front to a black body or gray body emission spectrum and assuming emissivity ϵ is independent of photon wavelength λ . Since these specimens were transparent, the optical emission is observed for several 100 ns while the shock front transits the specimen, as illustrated in **Fig. 6**. The effective emission temperature can be taken in many cases as the shock-temperature of the specimen. Results for transparent liquid D₂ are one example [15].

Because of the thin optical depths of opaque materials (~ 100 Å and \sim ps), direct shock temperature measurements on the Hugoniot are precluded by insufficient diagnostic temporal resolution. Temperatures of opaque solids are usually calculated as in II.C. In one case shock temperatures of metallic Fe have been measured by observing optical radiation from partially released Fe through a transparent diamond window, taking into account shock-wave reflections and thermal transport at the Fe/diamond interface [16].

II.E Shock-Wave Profiles

In shocked solids at pressures just above the HEL or just above phase-transition pressures, a shock wave has a macroscopic multiple-wave structure. By measuring time-resolved shock-wave profiles, EOS, mechanical constitutive properties and phase transition pressures are derived.

II.E.1 Elastic-Plastic Flow and Material Strength

Ideal elastic-plastic flow is illustrated in **Fig. 3**. For $P_A = P_{HEL} < P_C < P_B$, a two-wave structure propagates. Because elastic wave speeds are

greater than plastic ones, the elastic wave propagates as a precursor ahead of the plastic wave. The HEL is typically about a factor of 2 greater than the yield strength. P_{HEL} is given by

$$P_{HEL} = \frac{C_L^2}{2C_T^2} Y^0, \quad (3)$$

where P_{HEL} is the pressure of the Hugoniot elastic limit (commonly called the HEL), C_L and C_T are longitudinal and transverse sound speeds, and Y^0 is yield strength. The HEL's of Cu, hardened steel, alumina, and B_4C are about 0.3, 2, 10, and 15 GPa, respectively. HEL's are directionally dependent in anisotropic crystals.

A solid material with strength supports shear stress. As a result, the Hugoniot lies above the hydrostat in P-V space for a strong solid, stress is a more accurate representation than pressure, and stress is anisotropic. Stress in the direction of shock propagation is what is measured in a Hugoniot experiment. For a fluid, pressure and stress are identical. The principal stresses σ_i in a solid and the hydrostatic pressure P are given by

$$\sigma_i = -P + s_i, \quad i = 1, 2, 3 \quad (4)$$

and

$$-P = 1/3 (\sigma_1 + \sigma_2 + \sigma_3), \quad (5)$$

where the s_i are the stress deviators in the principle directions i and $\sum s_i = 0$. The yield strength Y^0 is such that

$$s_1^2 + s_2^2 + s_3^2 \leq (Y^0)^2. \quad (6)$$

For a perfectly plastic material, Y^0 is a constant independent of pressure. For many metals, called elastic-plastic, work hardening increases yield strength Y for shock stresses above the HEL. That is, as shock pressure increases the amount of plastic work and associated shock temperature, Y increases to a maximum and then decreases until $Y = 0$ at melting, where individual stress deviators $s_i = 0$ in the fluid state. For Cu, Y^0 is about 0.1 GPa and Y_{max} is about 2.5 GPa at 70 GPa shock stress and 1000 K shock temperature [17]. Cu melts at a shock pressure of about 230 GPa [18].

II.E.2 Shock-Induced Phase Transitions

Phase transitions are induced by dynamic high pressures and temperatures. If crystal volume changes at the transition, then pressure and material velocity change as well. By measuring time-resolved pressure or mass-velocity histories, phase changes can be detected. The graphite-to-diamond transition is an example. The P-V curve and wave structure are similar to those in **Fig. 3**, except that in this case P_A is the phase transition pressure, rather than the HEL. The measured velocity of an interface between shocked graphite and a LiF window is shown in **Fig. 7**. The first wave, or velocity jump, is graphite shock-compressed to 21 GPa. The second wave or velocity jump is caused by the transformation of graphite to diamond above 21 GPa, which occurs in 10 ns in the highly-ordered pyrolytic graphite specimen, oriented with its c axis of the hexagonal-graphite crystal structure parallel to the shock direction. The fast nature of the phase transition is the signature of a martensitic transformation [19]. The kinetics of this transformation are quite sensitive to the degree of crystalline order and to the relative crystallographic orientation of the specimen with respect to the direction of shock propagation. The velocity profile of **Fig. 7** was measured with a VISAR, or Velocity Interferometer for a Surface of Any Reflector [20]. Shock-wave profiles can be measured with a Fabry-Perot interferometer or with piezoelectric gauges, as well.

II.F Release of Shock Pressure by Longitudinal Sound Waves

A calculated temporal wave profile of a strong planar shock in Cu is shown in **Fig. 8** [21]. This shock is induced in a target by impact; a shock is also induced in the impactor and travels back toward the rear surface of the impactor (**Fig. 5**). On reaching the rear surface of the impactor, pressure drops and a longitudinal pressure release wave is transmitted forward into the impactor, eventually overtaking and releasing the original shock wave as it travels in the target. At overtake, pressure and temperature decrease at rates of 10^{12} bar/s and 10^9 K/s.

Shock pressure is also released by transverse sound waves which travel perpendicular to the direction of shock propagation. This release starts at the edge of a planar impactor and travels radially inward toward the axis of a planar sample. This transverse pressure release establishes an angle α whose tangent is the ratio of the distance of travel of release to the distance of travel of the shock at a given time time:

$$\tan \alpha = [c^2 - (u_s - u_p)^2]^{1/2} / u_s, \quad (7)$$

where c is sound speed [22].

II.F.1 Speed of Sound Measurements

The longitudinal pressure release wave described in II.F travels at the speed of sound c in the material, which is traveling at mass velocity u_p in the laboratory frame. Thus, the release wave travels at velocity $u_p + c$, which is greater than u_s . The longitudinal speed of sound C_L of a high-pressure shock state is determined by measuring the depth in the target at which the release wave just overtakes the shock, provided u_s and u_p are known [23]. Transverse sound speed is determined by measuring α at a given $u_s - u_p$ point.

II.F.2 Gruneisen Parameter and Phase Transitions

For the case of a fluid, the bulk thermodynamic speed of sound C_B is given by

$$C_B = V_H \{(\partial P / \partial V)_H [(V_0 - V_H) (\gamma / 2 V_H) - 1] + P_H (\gamma / 2 V_H)\}^{1/2}, \quad (8)$$

where the partial derivative is taken along the Hugoniot [24]. For this case, C_B is assumed equal to C_L . Thus, sound speeds measured in shocked fluids can be used to calculate $\gamma(V)$, which can be used to calculate off-Hugoniot states, as in II.C.

For the case of a solid with shear strength

$$C_B^2 = C_L^2 - (4/3) C_T^2. \quad (9)$$

Melting is often taken to occur at the shock pressure at which $C_L = C_B$, where C_L is measured and C_B is calculated from Eq. 8. Because the speed of sound is related to a derivative of pressure with respect to volume, sound speed is more sensitive to a phase transitions than Hugoniot $P_H - V_H$ relations.

II.G Electrical Resistivity

By inserting electrodes into a sample cavity, electrical resistance R of the sample cell is measured under shock compression. Electrical resistivity ρ is derived from the measured resistance via the geometrical factor C relating the two, $C=R/\rho$. The geometrical factor is obtained by experimental calibration and/or computational simulations.

Hydrogen becomes a metallic fluid at 140 GPa and 2600 K under dynamic compression by a shock reverberating between two stiff anvil crystals [25,26]. The resistivity of solid FeO at 100 GPa shock pressure is about 100 $\mu\text{ohm-cm}$ [27], which is in the range for metallic Fe at 100 GPa. The electrical resistivity of water has been measured up to 180 GPa using both single [28] and reverberating shock compression [29]. Protons are the charge carriers in shock-compressed water.

II.H Raman Spectroscopy

Raman spectroscopy has been used to observe shifts in the vibrational frequency of water [30] and of diamond [31] as a function of shock pressure. The Raman data for shock-compressed water indicate that as long as intermolecular hydrogen bonds are intact, water molecules also remain essentially intact. However, once intermolecular hydrogen bonds start breaking at 12 GPa shock pressure, water molecules begin to decompose continuously until only protons and hydroxyl ions are present at ~25 GPa.

II.I Flash X-Ray Diffraction

Flash x-ray diffraction has been performed on graphite, BN and LiF single crystals at shock pressures up to 100 GPa using both a two-stage gun and explosives to generate shock waves. The x-ray pulses had a width of ~50 ns. The observation of broad diffraction lines shows that the material has long-range crystalline order, as well as high densities of shock-induced lattice defects. By looking at various crystal orientations, the compression is isotropic within the uncertainties and the experimental x-ray density is equal to the Hugoniot density (Eq. 1b) up to 100 GPa shock pressures for LiF [32].

At lower pressures up to 4 GPa, shock compression of LiF is not isotropic. Shock compression along the [111] direction results in macroscopic elastic deformation which produces no transverse lattice deformation. In contrast shock compression along the [100] direction causes macroscopic elastic-plastic deformation which produces equal

changes in interplanar spacing in both the longitudinal and transverse directions [33].

By reducing the x-ray pulse width an order of magnitude to 5 ns, strengths of bonds are observed. X-ray diffraction with subns temporal resolution has been used to measure the lattice parameters of orthogonal planes in shock compressed single crystals of Si and Cu. Despite uniaxial compression along the (400) direction of covalent Si reducing the lattice spacing by ~11%, no observable changes occur in planes with normals orthogonal to the direction of shock compression. However, shock compression of metallic Cu is hydrostatic on this fast time scale. These results are consistent with the different types of bonding and the associated simple estimates of plastic strain rates based on dislocation velocities [34].

II.J Computational Simulations

Experimental data described above are used to develop material databases for EOS and constitutive properties for implementation into computer codes. These codes are called hydrodynamic, even for solids which have strength. Hydrodynamic codes are used to simulate, design, and interpret a variety of dynamic high-pressure experiments on a macroscopic scale. Quantum Molecular Dynamics, Quantum Monte Carlo, and electron-energy-band techniques are used to understand the nature of fluids and solids at high dynamic pressures on a microscopic (atomic, molecular, or lattice) scale. Macroscopic and microscopic theoretical calculations are essential to performing and understanding dynamic high-pressure experiments.

III. Materials Synthesized with High Dynamic Pressures

Dynamic high pressures are used to produce novel crystal structures, microstructures, and associated properties by subjecting specimens to dynamic pressures and recovering them intact for characterization. That is, pressure is applied at strain rates up to $10^8/\text{s}$ and higher, materials are shocked to pressures as high as 100 GPa and temperatures as high as a few 1000 K, held at pressure for $\sim\mu\text{sec}$, and quenched at rates up to 10^{12} bar/s and 10^9 K/s (**Fig. 8**). While pressure releases to zero, temperature releases to a residual value, which is higher than the initial value because of irreversible shock heating (**Fig. 4**). The residual temperature approaches the ambient value by thermal conduction into surrounding

material. These high quench rates mean that phases and structures synthesized at high shock pressures and temperatures might be quenched to ambient.

III.A Experimental Methods

A wide range of material effects are investigated in small specimens using a 6.5-m long two-stage light-gas gun and lasers. High explosives are used to synthesize diamond powders on a commercial scale.

III.A.1 Two-Stage Light-Gas Gun

Effects of dynamic high pressures in relatively small specimens are investigated using a two-stage light-gas gun. The gun [26] accelerates a planar metal projectile to a maximum impactor velocity of ~ 4 km/s with He driving gas, which produces 120 GPa (1.2 Mbar) for a Cu plate impacting a Cu target. Velocities up to 7 km/s could be achieved with H₂ driving gas, which would achieve ~ 400 GPa shock pressure in Cu. A shock is generated on impact of the projectile with a target capsule in which a specimen is embedded. Typical dimensions of a gun for this purpose are a length of 6.5 m and a bore diameter of 20 mm. Specimens are typically 10 mm in diameter and 0.001 to 1 mm thick. Initial temperatures can be varied in the range 100 to 1300 K [35]. A representative configuration is illustrated in **Fig. 9**. Materials shocked in this system and recovered intact have a variety of novel structures and properties, as discussed below.

III.A.2 Nanocrystalline Materials

Shock compression of single-crystal quartz causes the formation of polycrystalline grains, which facilitates flow of the bulk sample under rapid deformation at shock pressures of 20 to 50 GPa. As a result the grain boundaries reach very high heterogeneous temperatures, which reduce SiO₂ to Si and O, which in turn phase separate. Because the duration of maximum pressure in these experiments is a few 100 ns, there is sufficient time only for nanocrystalline Si (n-Si) particles to nucleate and grow in situ within the solid SiO₂. These nanoparticle have the well-ordered diamond crystal structure [36]. The size distribution of n-Si can be tuned by choice of shock pressure and its duration. The chemical history of this n-Si is completely different than that of samples made with traditional wet-chemistry methods, which might shed light on the

mechanism of their photoluminescence; that is, is photoluminescence caused by quantum confinement or oxygen passivation of the Si surface.

III.A.3 Films

High-pressure phases might be synthesized and quenched metastably. Nb films 1-10 μm thick have been recovered from 100 GPa shock pressure [37], demonstrating the feasibility of this process for very thin samples with maximum quench rates.

III.A.4 Bond Strengths Between Film and Substrate

The strength of bonding between a film made by conventional means and its substrate is measured by launching a short-pulse planar shock into a substrate, which then transits the film. The shock reflects as a tensile wave from the free surface of the film and travels back in the direction from which the original shock came. The tensile stress required to delaminate the film from the substrate is determined from the spall signal, that is, from the shape of the time-resolved free-surface velocity history of the film, which is measured with a fast optical velocimeter [20]. Short-pulse incident shock waves are generated by impact of thin metal foils [38] or by a laser [39].

III.A.5 Shock-Induced Defects and Fluxpinning

Shock deformation in ceramics induces dislocations and stacking faults, which pin magnetic flux and enhance magnetic hysteresis and magnetic levitation force in superconducting $\text{YBa}_2\text{Cu}_3\text{O}_{7-x}$. By using highly ordered melt-textured specimens and orienting their slip plane at 30° with respect to the shock direction, these brittle oxide specimens can be shocked without macroscopic fracture. After annealing the shocked specimen in oxygen to repair shock-induced damage in bulk, dislocations are converted into stacking faults. As a result the magnetic hysteresis, and thus critical current density, at 1 kOe and 70 K is about 20 % greater than the value before shock at 7 GPa [40].

Shock compaction of SmCo_5 particles at ~ 8 GPa enhances cohesive forces, increasing the “permanency” of this permanent ferromagnet [41].

III.A.6 Synthesis of Hard Materials

Potentially new hard materials can be synthesized and recovered from dynamic high pressures. For example, shock-compressed mixtures of C₆₀ fullerenes and Cu powders produce fine grained diamond [42]. Nanocrystalline metastable diamond films have been produced by shock compression of 2 μm thick C₆₀ fullerene films [43].

III.A.7 Powder Consolidation

Dynamic compaction rapidly consolidates powders by depositing compressive energy on particle surfaces, which are heated heterogeneously, often bond together, and then quench thermally to the interiors of the particles forming a dense compact. Advantages include: i) focussing energy on particle surfaces so that the whole system does not need to be heated for compaction; ii) consolidating powders so quickly that grains do not have time to grow nor do metastable phases have time to decompose; and iii) bonding powders of composite materials. Single-piece disks of both conventional and rapidly solidified alumina/zirconia ceramics have been consolidated by a reverberating shock wave [44]. A computational model has been developed for dynamic compaction which could be applied to a wide variety of materials, pressures, and consolidation rates and, thus, address key issues computationally [45].

III.A.8 Shock-Induced Chemical Reactions and Reactivity

Dynamic high pressures and temperatures cause chemical reactions between powder particles, whose nature depends on the strength of the shock wave. At relatively lower pressures, only powder surfaces are heated and, thus, this is a way to synthesize novel materials by high-temperature reactions localized at interfaces between powder particles. This is essentially what happens in dynamic powder compaction. In this case, however, the details of chemical reactions at interfaces are important, rather than the mechanical strength at interfaces required for a strong compact. Shock-induced defects cause higher chemical reactivity in bulk materials [46].

III.A.9 Shock-Induced Melting and Rapid Resolidification

Because powders have a lower initial density than a crystalline solid, powders are more compressible and, thus, have higher internal shock energies and higher shock temperatures at a given volume than do solid specimens. Thus, there is a range of relatively high shock pressures in which powders are readily shock melted in bulk and thermally quenched by thermal conduction into surrounding solid metals such as Cu. At relatively lower shock pressures powders are simply compacted dynamically by a shock as discussed in III.A.7. Model calculations have been used to predict that Cu-Zr powders would compact at 16 GPa and shock-melt at 60 GPa, as observed by experiment [47].

III.A.10 Explosive Systems to Synthesize Diamond Particles

Probably the best known example of materials produced commercially with dynamic pressure is the synthesis of diamond powders for abrasives [48]. This system is about 4 m long and about 1 m in diameter. A mixture of carbon and metal powders is placed inside a cylindrical explosive system, which drives the carbon into the pressure-temperature stability field of diamond. Polycrystalline diamond powders are synthesized from the carbon, which are quenched thermally by the metal powders before the pressure is released. Polycrystalline diamond is produced with a range of particle sizes of 0.1 to 40 μm .

ACKNOWLEDGMENT

This work was performed under the auspices of U.S. Department of Energy by the University of California Lawrence Livermore National Laboratory under Contract No. W-7405-ENG-48.

References

- [1] KEELER R. N. and ROYCE E. B., in *Physics of High Energy Density, Proceedings of the International School of Physics "Enrico Fermi", Course III*, edited by P. CALDIROLA and H. KNOEPFEL (Academic Press, New York) 1971, pp. 51-150.
- [2] McQUEEN R. G., MARSH S. P., TAYLOR J. W., and FRITZ J. N. in *High-Velocity Impact Phenomena*, edited by R. KINSLOW (Academic Press, New York) 1970, pp. 293-417.
- [3] HALL C. et al, *Rev. Sci. Instrum.* (in press).
- [4] KLIMENKO V. Y. and DREMIN A. N., in *Detonatsiya, Chernogolovka* (Academy of Sciences Press, Moscow) 1975, p.79.
- [5] HOOVER W. G., *Phys. Rev. Lett.*, **42** (1979) 1531.
- [6] BELAK J., in *Science and Technology of High Pressure* (Universities Press, Hyderabad) 2000, pp. 200-205.
- [7] RUOFF A. L., *J. Appl. Phys.*, **38** (1967) 4976.
- [8] McMAHAN A. K., *Bull. Amer. Phys. Soc.*, **21** (1976) 1303.
- [9] MARSH S. P., *Los Alamos Shock Hugoniot Data*, (University of California Press, Berkeley) 1979.
- [10] MITCHELL A. C. and NELLIS W. J., *J. Appl. Phys.*, **52** (1981) 3363.
- [11] McQUEEN R. G., MARSH S. P., TAYLOR J. W., and FRITZ J. N. in *High-Velocity Impact Phenomena*, edited by R. KINSLOW (Academic Press, New York) 1970, p. 300.
- [12] CARTER W. J., MARSH S. P., FRITZ J. N., and McQUEEN, R. G. in *Accurate Characterization of the High-Pressure Environment*, (National Bureau of Standards Press, Washington) 1971, pp. 147-158.
- [13] MITCHELL A. C., NELLIS W. J., MORIARTY J. A., HEINLE R. A., HOLMES N. C., and TIPTON R. E., *J. Appl. Phys.*, **69** (1991) 2981.
- [14] RUOFF A. L., XIA H., LUO H., and VOHRA Y. K., *Rev. Sci. Instr.*, **61**, (1990) 3830.
- [15] HOLMES N. C., ROSS M., and NELLIS W. J., *Phys. Rev. B*, **52** (1995) 15835.
- [16] YOO C. S., HOLMES N. C., ROSS M., WEBB D. J., and PIKE C., *Phys. Rev. Lett.*, **70** (1993) 3931.
- [17] MORRIS C. E. and Fritz J. N., *J. Appl. Phys.*, **51** (1980)1244.
- [18] MORIARTY. J. A., in *Shock Waves in Condensed Matter* (Plenum Press, New York) 1986, pp. 101-106.
- [19] ERSKINE D. J. and NELLIS, W. J., *J. Appl. Phys.*, **71** (1992) 4882.
- [20] BARKER L. M. and HOLLENBACH R. E., *J. Appl. Phys.*, **43** (1972) 4669.
- [21] NEUMEIER J. J., NELLIS W. J., MAPLE M. B., TORIKACHVILI M. S., YANG K. N., FERREIRA J. M., SUMMERS L. T., MILLER J. I., and SALES B. C., *High Pressure Res.*, **1** (1989) 267.

- [22]. ALTSHULER L. V., KORMER S. B., BRAZHNİK M. I., VLADIMIROV L. A., SPERANSKAYA M. P. AND FUNTIKOV A. I., *Sov. Phys. JETP*, **11** (1960) 766.
- [23] BROWN J. M. and McQUEEN R. G., *J. Geophys. Res.*, **91** (1986) 7485.
- [24] McQUEEN R. G., MARSH S. P., and FRITZ J. N., *J. Geophys. Res.*, **72** (1967) 4999.
- [25] WEIR S. T., MITCHELL A. C., and NELLIS W. J., *Phys. Rev. Lett.*, **76** (1996) 1860.
- [26] NELLIS W. J., *Sci. Am.*, **May** (2000) 60.
- [27] KNITTLE E., JEANLOZ R., MITCHELL A. C., and NELLIS W. J., *Solid State Comm.*, **59** (1986) 513.
- [28] MITCHELL A. C. and NELLIS W. J., *J. Chem. Phys.*, **76** (1982) 6273.
- [29] CHAU R., MITCHELL A. C., MINICH R. W., and NELLIS W. J., *J. Chem. Phys.*, **114** (2001) 1361.
- [30] HOLMES N. C., NELLIS W. J., GRAHAM W. B., and WALRAFEN G. E., *Phys. Rev. Lett.*, **55** (1985) 2433.
- [31] GUPTA Y. M., HORN P. D., YOO C. S., *Appl. Phys. Lett.*, **55** (1989) 33.
- [32] JOHNSON Q. and Mitchell A. C., in *High Pressure Science and Technology*, (Pergamon Press, Oxford) 1980, pp. 977-978.
- [33] RIGG P. A. and GUPTA Y. M., *Phys. Rev. B*, **63** (2001) 094112.
- [34] LOVERIDGE-SMITH A. et al, *Phys. Rev. Lett.*, **86** (2001) 2349.
- [35] GRATZ A. J., NELLIS W. J., CHRISTIE J. M., BROCIIOUS W., SWEGLE J., and CORDIER P., *Phys. Chem. Minerals* **19** (1992) 267.
- [36] FISKE P. S., NELLIS W. J., LIPP M., LORENZANA H., KIKUCHI M., and SYONO Y., *Science* **270** (1995) 281.
- [37] KOCH R., NELLIS W. J., HUNTER J. W., DAVIDSON H., GEBALLE T. H., *Pract. Met.* **27** (1990) 391.
- [38] NUTT G. L., *J. Mat. Res.*, **7** (1992) 203.
- [39] GUPTA V., YUAN J., and MARTINEZ D., *J. Am. Ceram. Soc.* **76** (1993) 305.
- [40] NELLIS W. J., WEIR S. T., HINSEY N. A., BALACHANDRAN U., KRAMER M. J., and RAMAN R., in *High-Pressure Science and Technology-1993*, edited by S. C. SCHMIDT, J. W. SHANER, G. A. SAMARA, and M. ROSS (American Institute of Physics Press, New York) 1994, pp. 695-697.
- [41] CHAU R., MAPLE M. B., and NELLIS W. J., *J. Appl. Phys.* **79** (1996) 9236.
- [42] SEKINE T., *Proc. Japan Acad. Ser. B.* **68** (1992) 95.
- [43] YOO C. S., NELLIS W. J., SATTler M. L., MUSKET R. G., *Appl. Phys. Lett.*, **61** (1992) 273.
- [44] FREIM J., McKITTRICK J., and NELLIS W. J., in *High-Pressure Science and Technology-1993*, edited by S. C. SCHMIDT, J. W. SHANER, G. A. SAMARA, and M. ROSS M. (American Institute of Physics Press, New York) 1994, pp. 1263-1266.
- [45] BENSON D. J. and NELLIS W. J., *Appl. Phys. Lett.*, **65**, (1994) 418.

- [46] BERGMANN O. R. and BARRINGTON J., *J. Am. Cer. Soc.*, **49** (1966) 502.
- [47] NELLIS W. J., GOURDIN W. H., and MAPLE M. B., in *Shock Waves in Condensed Matter-1987*, edited by S. C. Schmidt and N. C. Holmes (Elsevier, New York) 1988, pp. 407- 410.
- [48] COWAN G. R., DUNNINGTON B. W., and HOLTZMAN H. A., (1968), *U. S. patent 3,401,019*.

FIGURES

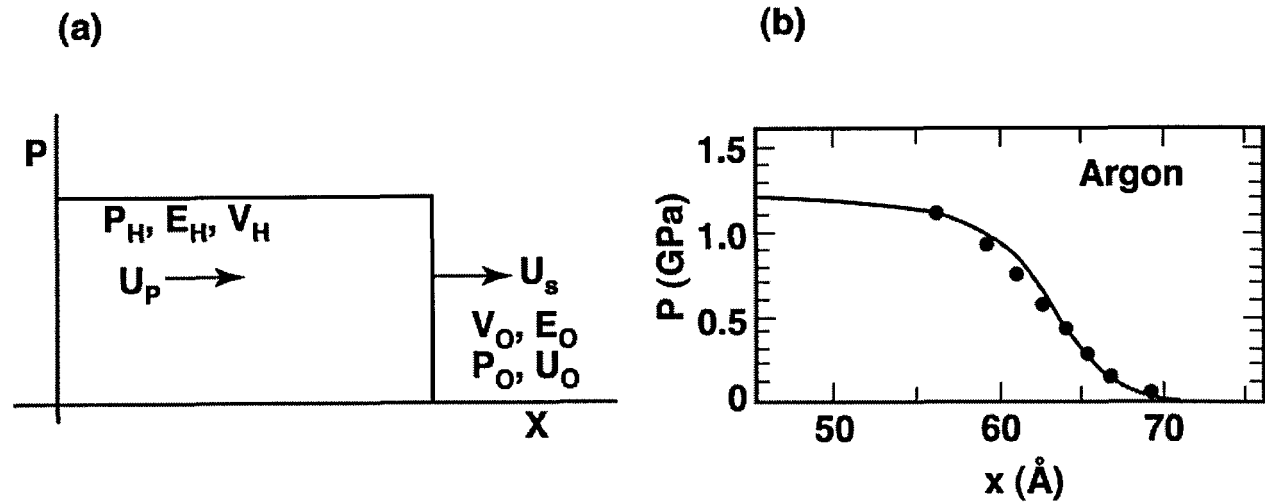


Figure 1. (a) Schematic of simple shock wave travelling at velocity u_s in x direction. Shock is essentially traveling discontinuity. (b) Spatial rise of pressure to 1.2 GPa in 10 Å at shock front in argon; shock speed is 1.8 km/s. Full curve was calculated with atomistic molecular dynamics [4]; dots were calculated with the Navier-Stokes equations [5]. Shock front is thicker in system with more degrees of freedom than simply intermolecular repulsion.

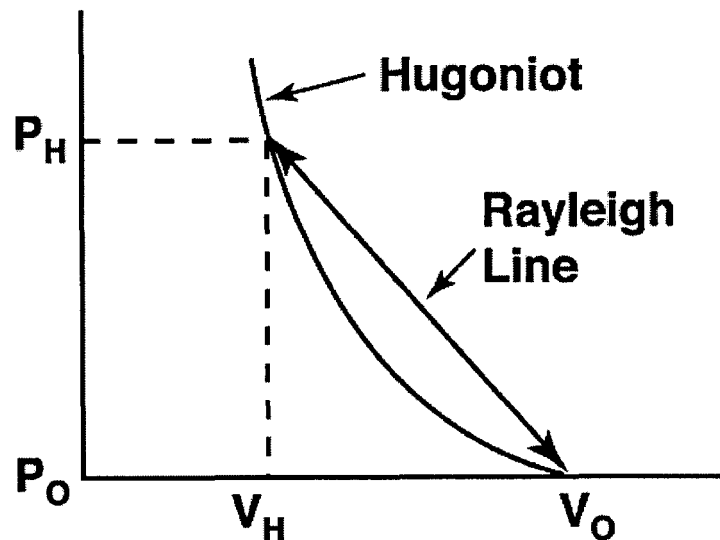


Figure 2. Illustration in P - V space of shock compression of material initially at V_0 to a P_H - V_H point on Hugoniot curve. Loading is along Rayleigh line joining initial and final states. Hugoniot is locus of P_H - V_H states.

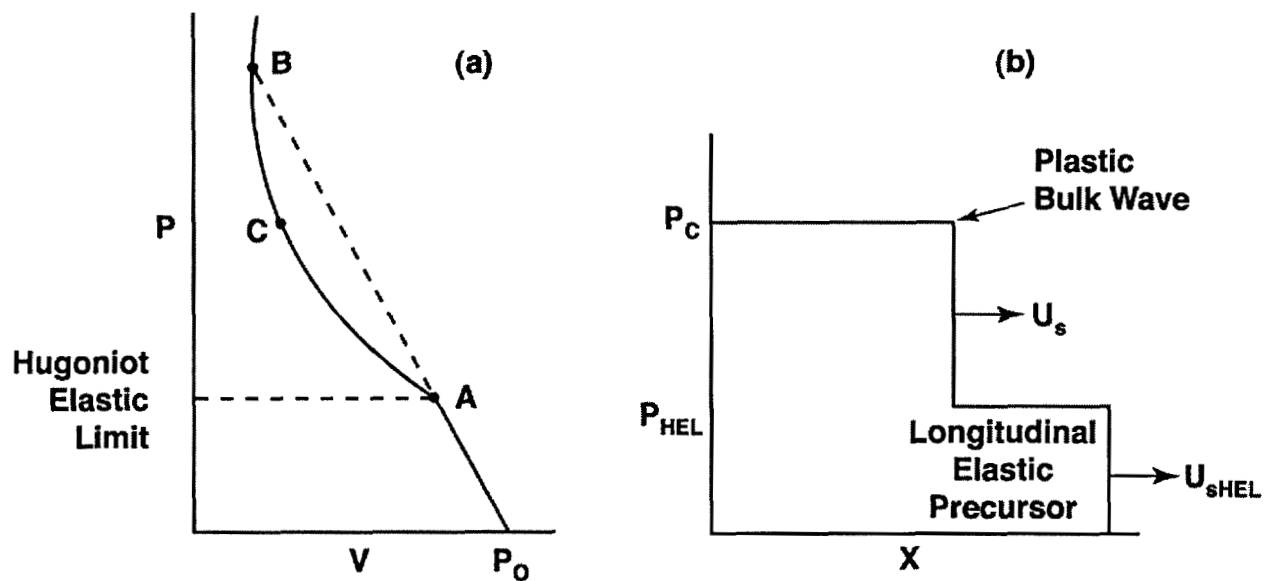


Figure 3. (a) Hugoniot of solid with Hugoniot elastic limit, $P_A = P_{HEL}$. P_B is minimum shock pressure required to overdrive HEL, that is, to achieve a single plastic shock wave. (b) At intermediate pressure P_C , two-wave structure propagates. Elastic precursor at P_{HEL} travels at the longitudinal sound speed C_L , followed by a plastic shock traveling at shock velocity u_s .

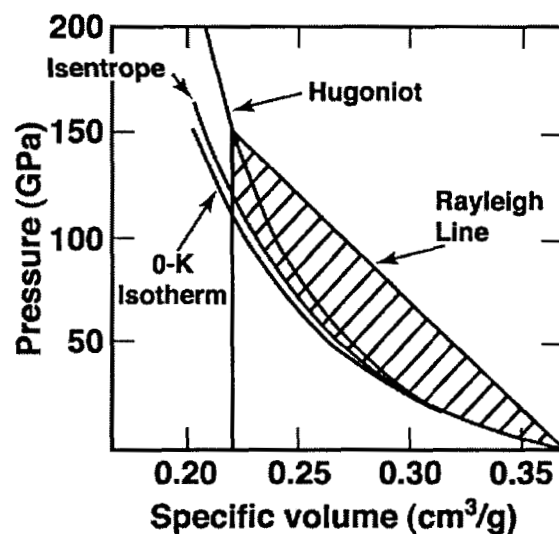


Figure 4. Illustration of irreversible internal energy (shaded region) in shock compression. This example is for Al shocked to 150 GPa and shows measured Hugoniot, calculated O-K isotherm, and isentrope from crystal volume [7].

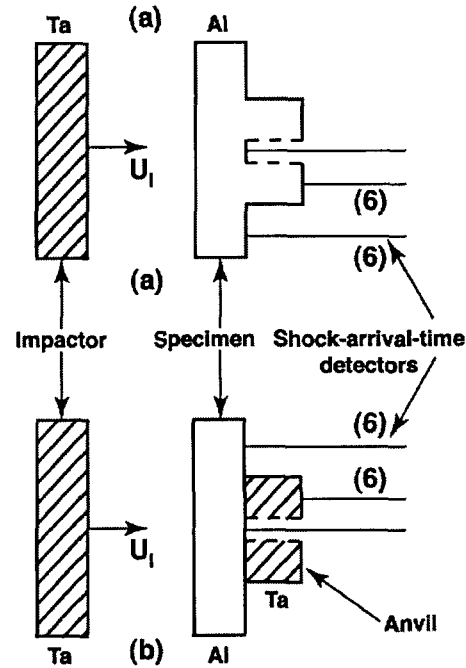


Figure 5. Illustration of (a) single-shock and (b) double-shock EOS experiments. Velocity of inflight impactor is measured with flash radiography; shock velocity in target is measured by measuring shock transit time across measured step height with array of point detectors [9].

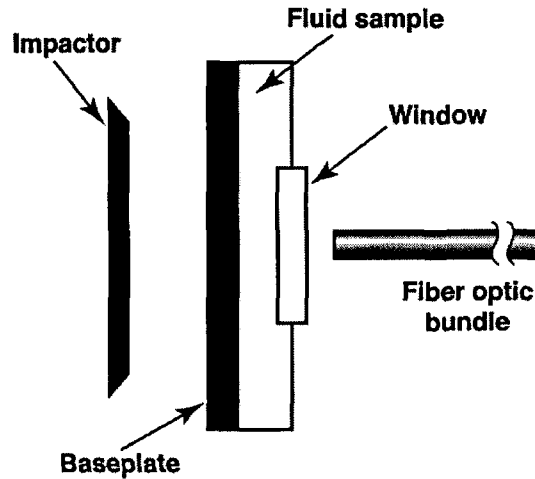


Figure 6. Schematic of experiment to measure shock-induced radiation temperatures. Impactor is incident from left and generates shock in baseplate. When shock enters fluid, sample becomes luminous. Fiber optic bundle collects light emitted from shock front, which passes through transparent unshocked fluid and window. First shock in fluid reflects off stiff window crystal producing higher shock pressure, temperature, and density [13].

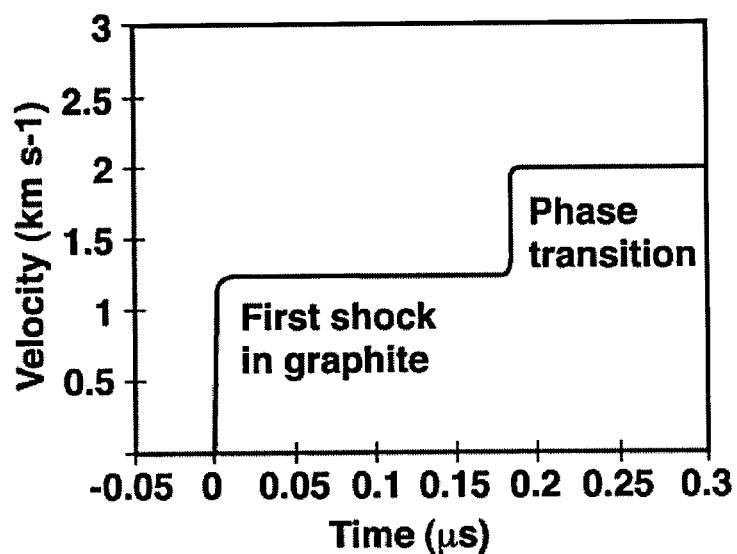


Figure 7. Measured wave profile in highly oriented pyrolytic graphite shocked into region of phase transition to diamond [17]. First knee is caused by elastic compression of graphite at 21 GPa; second knee is caused by phase transition to diamond.

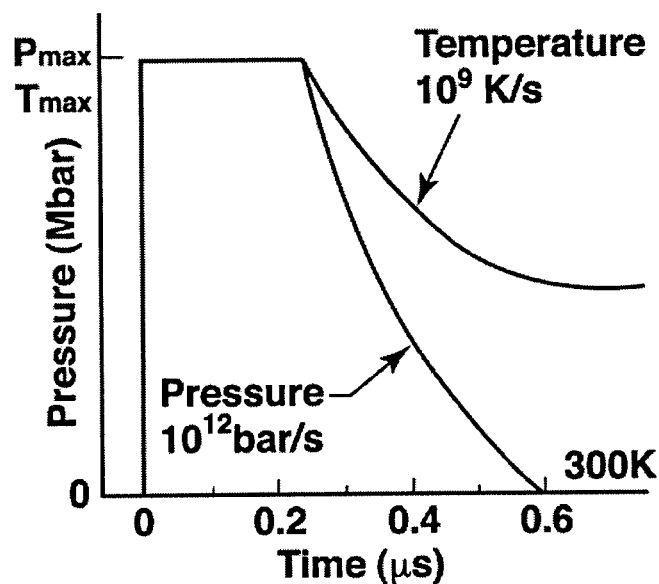


Figure 8. Shock and release profiles calculated in planar geometry for shock-compressed Cu. Pressure releases to zero but temperature does not because of irreversible internal shock energy shown in Fig. 5 [19].

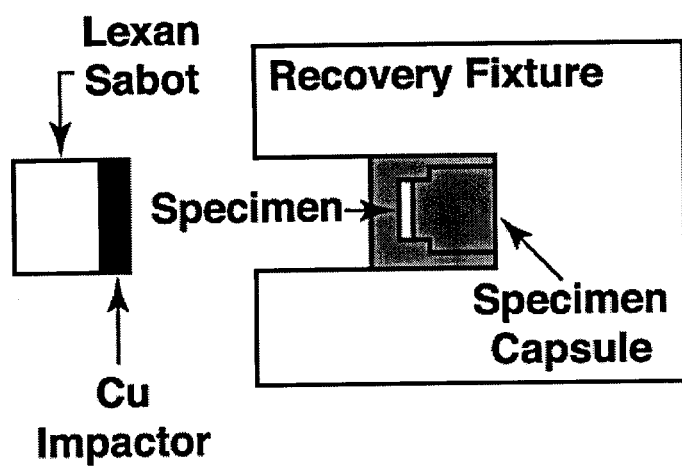


Figure 9. Schematic of an experiment to recover specimen shocked to high pressures up to 100 GPa. Projectile is launched by gas gun [33].